4D imaging and quantification of pore structure modifications inside natural building stones by means of high resolution X-ray CT

J. Dewanckele, T. de Kock, M. A. Boone, V. Cnudde, L. Brabant, M. N. Boone, Gilles Fronteau, L. van Hoorebeke, P. Jacobs

To cite this version:

J. Dewanckele, T. de Kock, M. A. Boone, V. Cnudde, L. Brabant, et al.. 4D imaging and quantification of pore structure modifications inside natural building stones by means of high resolution X-ray CT. Science of the Total Environment, 2012, 416, pp.436-448. ⟨10.1016/j.scitotenv.2011.11.018⟩. ⟨hal-01689088⟩

HAL Id: hal-01689088
https://hal.science/hal-01689088v1

Submitted on 25 Jan 2018

Dewanckele J., De Kock T., Boone M.A., Cnudde V., Brabant L., Boone M.A, **FRONTEAU G.,** Van Hoorebeck L., Jacobs. P. 2012. 4D imaging and quantification of pore structure modifications inside natural building stones by means of high resolution X-ray CT. *Science of The Total Environment*. 416. p 436-448. https://doi.org/10.1016/j.scitotenv.2011.11.018

4D imaging and quantification of pore structure modifications inside natural building stones by means of high resolution X-ray CT

J. Dewanckele [a,*], T. De Kock [a], M.A. Boone [a], V. Cnudde [a], L. Brabant [b], M.N. Boone [b], G. Fronteau [c], L. Van Hoorebeke [b], P. Jacobs [a]

a: Department of Geology and Soil Science — UGCT, Ghent University, Krijgslaan 281 S8, B-9000, Ghent, Belgium

b: Department of Physics and Astronomy — UGCT, Ghent University,

c: University of Reims Champagne-Ardenne (URCA), GEGENAA, EA3795, Reims, France

Abstract

Weathering processes have been studied in detail for many natural building stones. The most commonly used analytical techniques in these studies are thin-section petrography, SEM, XRD and XRF. Most of these techniques are valuable for chemical and mineralogical analysis of the weathering patterns. However, to obtain crucial quantitative information on structural evolutions like porosity changes and growth of weathering crusts in function of time, non-destructive techniques become necessary. In this study, a Belgian historical calcareous sandstone, the Lede stone, was exposed to gaseous SO2 under wet surface conditions according to the European Standard NBN EN 13919 (2003). Before, during and after the strong acid test, high resolution X-ray tomography has been performed to visualize gypsum crust formation to yield a better insight into the effects of gaseous SO2 on the pore modification in 3D. The tomographic scans were taken at the Centre for X-ray Tomography at Ghent University (UGCT). With the aid of image analysis, partial porosity changes were calculated in different stadia of the process. Increasing porosity has been observed visually and quantitatively below the new superficial formed layer of gypsum crystals. In some cases micro-cracks and dissolution zones were detected on the grain boundaries of quartz. By using Morpho+, an in-house developed image analysis program, radial porosity, partial porosity, ratio of open and closed porosity and equivalent diameter of individual pore structures have been calculated. The results obtained in this study are promising for a better understanding of gypsum weathering mechanisms, porosity changes and patterns on natural building stones in four dimensions.

Keywords: Weathering, Pore structure, X-ray CT, Gypsum crust, Natural building stone, Image analysis

1. Introduction

It is common knowledge that natural building stones disintegrate, due to weathering processes between the rocks' internal factors or geological parameters (pore structure, mineralogy, compaction,…) and the environment to which they are exposed (Camuffo, 1995). Most of the time the disintegration involves a complex progression from fresh to failed state (Warke and Smith, 2007). The environmental physical and chemical agents for stone weathering (rain, pollution, temperature, wind etc.) cause changes in the petrophysical properties of rocks, which often results in esthetic problems, combined with a decrease of durability (Camuffo, 1995). Naturally, the type of weathering is different for each type of rock and depends also on the location in the building or monument. In almost all deterioration processes, water or moisture is involved. The liquid can penetrate through pores, microcracks and capillaries into the mass of the stone and starts to degrade it by crystallizing salts into the pore spaces or by dissolving calcareous cement. Deterioration of historic building stones due to wet or dry pollutant deposition has been studied previously by many different authors, in field studies (Maravelaki-Kalaitzaki and Biscontin, 1999; Montana et al., 2008; Nord and Holenyi, 1999; Siegesmund et al., 2007; Smith et al., 2003; Torok and Rozgonyi, 2004) and laboratory investigations (Ausset et al., 1996; Giavarini et al., 2008; Sabbioni et al., 1996). Quantification of the induced damage is often obtained by indirect non-destructive measurements like mass loss weighing, visual inspection, superficial observations, sound speed propagation, etc. However, as most techniques developed to obtain a deeper insight into the finally failed situation are destructive, for example thin section petrography, scanning electron microscope (SEM) measurements, drilling resistance, mercury porosimetry, etc., further research on the same sample thus becomes impossible. Environmental scanning electron microscope (ESEM) can provide an alternative, although in this case only visual superficial features can be studied. Because of the heterogeneity of natural stones, the same sample must be considered in order to obtain direct pore evolution results. The growing interest in monument conservation and restoration underlines the need for highly detailed quantification of weathering processes in 3D. Although recent studies are encouraging (Christe et al., 2011; Cnudde et al., 2009a, 2011; Rozenbaum et al., 2007; Thomachot-Schneider et al., 2008), little data is available on the direct response of micro-structural changes such as pore structure evolutions. Moreover, limited research has been conducted on the interaction of weathering processes on three dimensional evolutions of those pore structure changes and their quantification on the same sample.

The key objective of this study is the use of high resolution X-ray computed tomography (X-ray CT) and 3D image analysis to obtain crucial information about gypsum crust formation, blistering and pore structure changes in a calcareous sandstone. Although this technique has been successfully used to investigate pore structures in geomaterials, little data is available on time-lapse quantification of induced weathering processes. In this study, several X-ray CT scans of the same sample were taken with a laboratory based X-ray source (Masschaele et al., 2007). This was done by degradation of calcareous sandstone samples in a laboratory environment according to the European Standard NBN EN 13919 (2003). The great advantage of this approach is the possibility to measure changes in porosity, evolutions of micro-cracks and disintegration in the same rock sample over a specific time period. Moreover, the relationship between days of weathering and pore network evolution is investigated here with a resolution of 2.5 µm. This research focuses on the quantification of altered pore structures due to gypsum crust formation using high resolution X-ray CT and image analysis rather than on the role of the gypsum crust in the deterioration process itself.

2. Materials and methods

2.1 Lede stone

The Lede stone is an important historical building stone in Belgium and the Netherlands. The stone originates from the Lede Formation (Lutetian, middle-Eocene) and was excavated in different quarries between Ghent and Brussels (Fig. 1). The term Balegem stone is a more specific name for the Lede stone, referring to the only active quarry left in the Schelde–Dender interfluvium (number 1 in Fig. 1). The Lede stone can be described as a calcareous sandstone or a sandy limestone, depending of its carbonate content, which fluctuates between 40% and 70% and consists of cement and fossils (Fobe, 1990). Commonly, the latter are fragments of echinoderms such as fossilized parts of sea urchins, gastropods, bivalves, foraminifers and serpulids. Besides the quartz fragments, the stone also contains small pyrite and glauconite grains. The microscopic texture varies between being without structure toward a laminated packstone and a bioclastic packstone or grainstone with a variable degree of bioturbation (Dusar et al., 2009). The macroporosity of the stone is very heterogeneous due to changing intensities of cementation and varies between 6 and 8% at the top and bottom to 1–1.5% in the core of the stone layer (Dusar et al., 2009).

The reason for choosing the Lede stone for this study is (1) its important historical value in Belgium and the Netherlands and (2) its weathering phenomena (both in patina creation as well as the formation of gypsum crusts). Generally, a fresh, unweathered, Lede stone has a light green-yellow to grayish-green color. However, the same sample exposed over a period of time to a polluted humid environment displays a more brownish-yellowish rust-colored patina, particularly caused by the oxidation of iron-bearing glauconite and pyrite (Fobe, 1990). In an urban environment the

Lede stone is also strongly subjected to crust formation. Acid rain, whether or not in combination with airborne particles and oxides of nitrogen, causes gypsum crusts to be formed. Due to the chemical weathering process, both esthetic and, in some severe situations, stability problems occur. In the case of mechanical weathering, like freeze–thaw cycles, those gypsum blisters can rapidly peel off (Dusar et al., 2009). Nevertheless, the Lede stone is one of the most frequent used historical building stones in the NW part of Belgium. For this study, two samples of Lede stone, Lede 1 and Lede 2, were used for the quantification and characterization with X-ray CT.

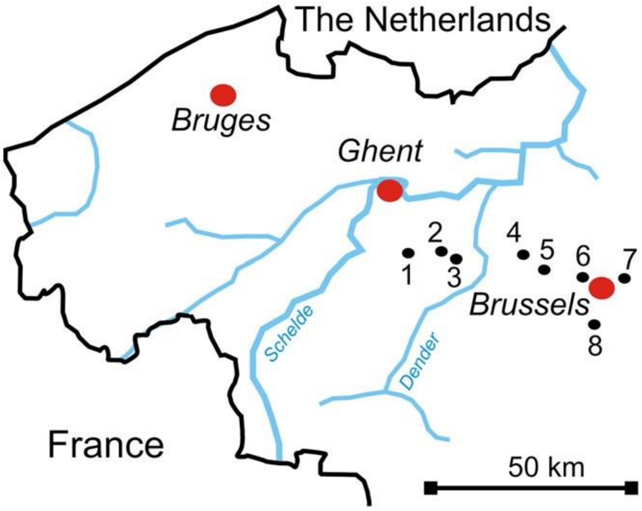

Fig. 1. Location map of the most important quarries of the Lede stone in Belgium, of which only the quarry in Balegem (1) is still active. 1: Balegem, 2: Vlierzele, 3: Bambrugge, 4: Meldert, 5: Asse, 6: Dieleghem, 7: Diegem, 8: Ukkel.

2.2 Gypsum crust formation

A large number of studies have been devoted to the problems concerning gypsum ($CaSO_4 \cdot 2H_2O$) crystallization because it is one of the most frequent minerals found in the crusts on historical monuments. The low mobility of gypsum favors its accumulation inside porous materials and at the surface of less porous media in comparison to other salts (Charola et al., 2007). The main aggressor in the process of gypsum crystallization on limestones is sulfur dioxide gas (SO_2). This gas is highly soluble in water and reacts with water by forming sulfurous acid (H_2SO_3). The reaction path for the attack on limestone is:

$CaCO_3 - \rightarrow CaSO_3 \cdot {}^{1} = {}_{2}H_2O$ ð1Þ

SO_2þH_2O

$CaSO_3 \cdot {}^{1}2H_2O - \rightarrow CaSO_4 \times 2H_2O$ ð2Þ

O_2þH_2O

Another possibility is the oxidation of sulfurous acid by oxygen (O_2) to form sulfuric acid (H_2SO_4). In the presence of water, this acid can dissolve calcium carbonate to form gypsum:

$CaCO_3$ þ $H_2SO_4 {}^{\rightarrow} 2$ $CaSO_4 \cdot 2H_2O$ ð3Þ

H O

The slightly soluble gypsum can be removed from the external part of the stone by rain. In this case, the stone remains in a clean state and erodes slowly. In the case of a sheltered part of a façade, the acid in the polluted air will continually condense on the wet surface. As a result, those areas can see the growth of a thick gypsum crust that becomes less and less permeable. In other words, the first formed gypsum crystals will prevent the structure below from continuing erosion. Those surfaces often become black because of the incorporation of pollution particles. Over time, those thick crusts can gradually peel off or form blisters. These phenomena are frequently found on less resistant limestones and calcareous sandstone, such as the Lede stone, as can be seen in Fig. 2. The stone surface immediately behind the blister is fragile and will therefore be preferentially vulnerable for further acid attack (Fig. 3).

Fig. 2. Formation and eruptions of blisters on the Lede stone surface (Saint Bavo's Cathedral, Ghent, Belgium).

As described in the Section 3, in this study, a gypsum crust is obtained after 10 days of exposure to an SO_2 rich environment, after which a second degradation step is induced to evaluate the further changes in the gypsum crust and in the pore structure. The formation of gypsum crystals requires the use of calcium carbonate. The resulting empty spaces inside the stone are indicated as zones of dissolution.

2.3 Strong acid test

In this study, several samples and subsamples of the Lede stone were subjected to the strong acid test. According to the European Standard NBN EN 13919 (2003), the samples were put in an acid environment for 21 days inside a closed plastic container of 50±5 l capacity. By putting a porous plastic plate on 10 cm high blocks inside the container, a stable permeable bottom for the samples was obtained. Underneath the bottom, a mixture of 500±10 ml H_2SO_3 and 150±10 ml de-mineralized H_2O was added. No airborne particles or oxides of nitrogen (NO_x) were added. The relative humidity in the plastic container amounted to more than 90%RH and the temperature was kept at 20±5 °C. Before putting the samples in the acid environment, water impregnation was performed. Two cylindrical samples (diameter 1.6 mm) of Lede 1 and Lede 2 were scanned with high resolution X-ray CT. Before the weathering test, and after 10 and 21 days of weathering, the porosity and dimensional changes were measured using image analysis. A schematic overview of the set up and strategy is given in Fig. 4.

Fig. 3. Weathering pattern of the Lede stone at the Saint Bavo's Cathedral (Ghent, Belgium), where the black gypsum crust is visible and is peeling-off.

After 10 days of exposure, both samples were removed from the acid environment and placed in a ventilated oven of 60 °C. After this first degradation step, a gypsum crust was formed on the surface of the samples. In a next step, the deteriorated samples were placed again in the acid environment for 11 days, corresponding to a total of 21 days of exposure. In this paper, after 10 and 21 days, respectively, refer to those two degradation steps.

2.4 High resolution X-ray tomography

High resolution X-ray CT allows 2D and 3D reconstructions of the internal structure of an object with a resolution of around 1 µm and even better (Cnudde et al., 2009b). The images to be formed are based on the attenuation of the X-ray through the object. Generally, the basic principles of high resolution X-ray CT are the same as for medical CT. Sample rotation instead of source-detector rotation and resolution improvement are the most innovative adaptations. Nowadays, X-ray CT has become a powerful tool in material research and has already been successfully applied in the field of natural building stone research (Christe et al., 2011). The experiments in this study were carried out at the Centre for X-ray Computed Tomography (UGCT; Ghent University, Belgium). For technical information on the open type device scanner, the reader is referred to the literature (Masschaele et al., 2007; Vlassenbroeck et al., 2007b).

For both samples a total of 1000 projections were registered over an angle of 360°. To reduce the noise factor, 6 frames were taken for each projection with an exposure time of 500 ms. A voltage of 80 kV and a tube current around 32 µA was installed and the obtained resolution for both samples was 2.5 µm. Taking this voxel size into account, features smaller than 2.5 µm were not visible in the reconstructed slices. The obtained raw CT data is afterwards processed with the in-house developed reconstruction software Octopus to remove dark and bright spots and normalize and regroup into sinograms (Dierick et al., 2004). For 3D visualizations, VGStudio 2.0 (Volume Graphics) was used.

Because the same samples had to be scanned three times (before, during and after the acid test), the challenge in this research was to match the 3D structural information of each scan. Therefore, the same acquisition parameters (filter, exposure time, amount of frames, etc.) were used for each scan. In addition, the same reconstruction parameters, like beam hardening correction, normalization, ring and spot filter, etc. were performed. The exact positioning of the sample for the different scans was obtained by saving the absolute position on the magnification stage. In this case, the same magnification and thus resolution of 2.5 µm was obtained for each scan.

2.5 Image analysis

Besides qualitative visual inspection and interpretation, quantitative data acquisition is an important aspect. To calculate the porosity change below the gypsum layer after 10 and 21 days of exposure, the reconstructed images were analyzed with the software program Morpho+ (Brabant et al., 2011; Vlassenbroeck et al., 2007a). This program enables segmentation of the features of interest, in this case the pore structure. Total porosity can be calculated on the cross-sections by thresholding the pores and interconnectivity of the pore structure. Open and closed porosity can be obtained after labeling. The porosity as a function of depth or position inside the sample, is the partial porosity. To calculate this partial porosity, several possibilities exist. The most common way to calculate the partial porosity is in the z-direction, thus in function of the height of the sample. Depending on the structure under investigation, calculation of the partial porosity in the x- and ydirection is also possible. Partial porosity changes of the Lede stone were calculated on both Lede 1 and Lede 2, in the three main directions x, y and z.

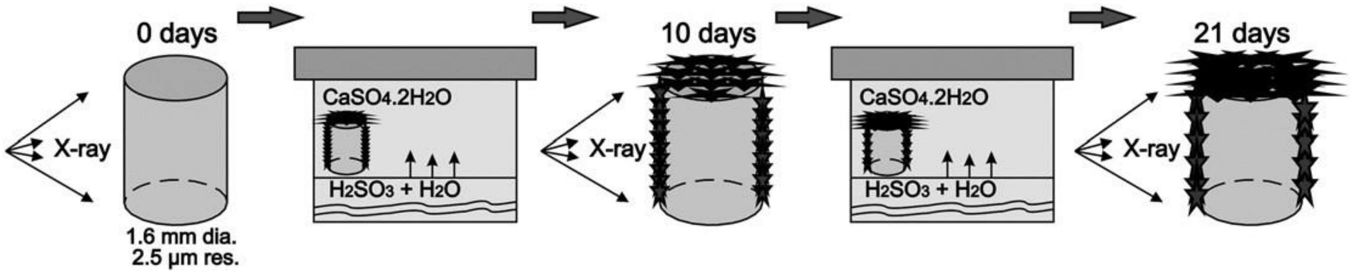

Fig. 4. Overview of the research set-up. A cylindrical core of 1.6 mm diameter has been scanned with X-rays before, during and after a strong acid test. The obtained resolution for each scan measures 2.5 µm.

To segment the pore structure from the stone material a dual thresholding was performed using Morpho+, where for each sample the same thresholding had to be performed on the images taken before, during and after the acid test. In every case a certain gray value was selected by using a dual threshold operation. Although similar acquisition and reconstruction parameters were chosen for each scan, effects like fluctuation of the X-ray intensity with time could have influenced the measurement results. Furthermore, the sample acquires a gypsum crust, resulting in different X-ray attenuation values and beam hardening. Taking this into account, the reconstructed cross-sections may show small variations in average gray value. Therefore, for each segmentation, different threshold values were used to calculate the partial porosity. To tune the thresholds to each other, the same slice and pore structure was used for calibration. To reduce beam hardening, a thin (500 µm) Al-filter was used for all the scans. In addition, within the reconstruction module, the effect of beam hardening was minimized using the beam hardening correction method in Octopus (Dierick et al., 2004).

Fig. 5a and b show a schematic overview of the partial porosity measurements for a cylindrical sample with a porous tube (shown in gray) inside the stone material (shown in yellow). The porous tube is present in the entire sample and represents a simplification of the coeval porous layer below the gypsum crust. In these figures, the porosity is calculated on three slices (slice 1, 2, 3) through the object in z- and x-direction (Fig. 5a,b). In this cylindrical shaped sample, the surface area of each slice in the z-direction is constant. On the other hand, if the partial porosity is calculated in the y- or x-direction, the calculated surface area differs from the border to the center. Therefore, a pore structure near the edges of the cylinder will affect the total porosity on that specific cross-section in the x- or y-direction, and thus also the partial porosity, more than the same pore structure in the center of the sample. In case of the coeval porous tube, the geometry will affect the partial porosity, resulting in a high porosity on the border and a gradual decrease toward the center.

In reality, deterioration and crust formation take place on the entire surface of the sample, as schematically shown in Fig. 5c. This figure illustrates a random cross-section in the x-direction. To calculate the partial porosity in either x- or y-direction for this type of sample there is no change, as can be seen on Fig. 5b and a and the results will still be affected by the geometry as described above. However, if the partial porosity is measured in the z-direction, the top part will now also be affected by the curved geometry of the sample.

To evaluate the calculations in the three main directions (x, y and z), the radial porosity has also been measured. In this case the porosity is calculated for a shell with adjustable thickness. By virtually eroding the sample and thus measuring the porosity from the outer borders of the sample toward the core, the porosity is measured as a function of depth. In this case, the results are not affected by the geometry due to the gradual, virtual eroding process from the outer border of the sample to the center. However, deeper inside the sample the regions of interest or shells become so small, making it very difficult to link different shells with each other. Therefore, little relevant information is obtained from the center of the sample. In addition, the curvature of the formed gypsum crystals highly determines the curvature of the shells deeper inside the sample and less at the border of the sample. However, this technique is ideal for changes that occur on the surface of the sample. As described, each approach toward calculation pore structure change has its advantages and disadvantages and a combination of different approaches is mandatory.

In addition, after the labeling process, the equivalent diameter (ED) of each pore structure was calculated. The interpretation of the ED can be explained by the length of the diameter of a sphere which has the same amount of voxels as the pore structure under investigation.

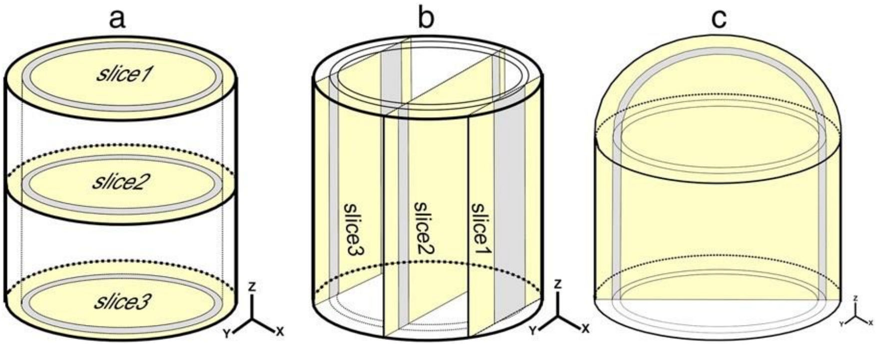

Fig. 5. Schematic overview of the quantitative interpretation of partial porosity measurements in a cylindrical sample in the z- and y-directions. The gray zone represents a porous cylinder that simulates the porous layer below the gypsum crust while the yellow color represents the stone material. (a) illustrates the calculation of the porosity in the z-direction on three different slices. (b) shows the calculation of the pore structure in the y-direction, also on three different but well-chosen cross-sections. The porosity in the z-direction will be the same on each slice while the partial porosity calculation in the y-direction will be dependent on the distance from the border of the cylinder. (c) shows a more realistic situation, where the entire surface of the sample including the top is deteriorated by the formation of a porous layer.

2.6 Sample size and preparation

In accordance with the standard test of strong acid assessment, the cuboid samples should have had a dimension of 120×60×10±

2 mm (EN 13919:2003). However, to obtain very high resolutions with X-ray micro-CT in a cone beam configuration, such sample size and shape are problematic for several reasons. Generally, the resolution (R) for cone beam geometry is expressed by the following equation:

$$R = \frac{d}{M} + \left(1 - \frac{1}{M}\right)s \qquad (4)$$

in which M is the magnification, d the resolution of the detector and s the spot size of the X-ray source. The magnification can be determined by the ratio of the source–detector distance over the source– object distance. For a cuboid sample with a dimension of 120 mm, the source–object distance will be larger compared to a few millimeters sized sample. According to Eq. (4), a shorter source–object distance results in a better resolution for smaller samples. So, if micrometer-scaled weathering features in natural building stones have to be detected with X-rays, sample sizes have to be decreased to several millimeters.

A second limitation with cuboid samples of centimeter size is the transmission of the X-rays through the material. With an average energy of 100 kV, the transmission of the X-ray through a block of $CaCO_3$ is limited. In the case of a thickness of $CaCO_3$ of several centimeters, the transmission will be insufficient for a good reconstruction. Furthermore, the use of higher energy beam needed for large samples, implies a higher focal spot and less contrast in attenuation and may thus lead to insufficient differentiation between crucial stone features. In addition, beam hardening artifacts, which cause the edges of the reconstructed slices to be lighter than their centers, will interfere more in cuboid samples than in cylindrical samples (Ketcham and Carlson, 2001).

Considering these limitations and the need for a high resolution, two cylindrical samples, “Lede 1” and “Lede 2” both with a diameter of 1.6 mm, were drilled in a fresh block of Lede stone and used for the ageing tests. Because of the dynamic concept of the tests, the position of the sample has to be stable during the scan over a period of time. In addition, during the acid test, the samples have to stay fixed. Several sample holders have been tested at UGCT and it turned out that a pencil lead is the most comfortable option to hold small samples steady during scanning. The attenuation of the carbon stick is also negligible in comparison to the attenuation of the stone. Hence, after drilling and drying, the samples were attached on top of a pencil lead. In addition, cuboid samples were cut in accordance with the standard procedure. Those cuboid samples underwent the same degradation tests and were used for visual, as well as for thin section microscopic investigations. High resolution X-ray CT and SEM measurements were performed on both small cylindrical samples Lede 1 and Lede 2.

2.7 Microscopic techniques

Both SEM and petrographic microscopy were used to analyze the weathered samples in addition to the high resolution X-ray CT scans. After the induced weathering tests, the cuboid set of samples was imbedded in epoxy, cut and prepared for thin section microscopy. The embedding in epoxy was done to preserve the fragile gypsum layer. The images and results of the polarization microscopy study were afterwards compared with the high resolution X-ray CT scans for a better interpretation of the 3D image analyses results. SEM visualization was performed both on the top surface of the cylindric Lede 1 surface (JEOL JSM 6400) and on an internal surface. The results of SEM were obtained on the final modified samples (after 21 days), after the samples were scanned with X-ray CT. By embedding, cutting and polishing, the internal surface was obtained and could be linked with the slice obtained by high resolution X-ray CT. In addition EDS measurements were performed to locate the gypsum inside the rock sample.

3. Results

3.1. Visual observation of reconstructed slices and 3D volumes

In order to obtain quantitative data about the gypsum crust formation processes, 3D image analysis is required. The first step in the complex path of the image analysis is having a good overview of features under investigation. Therefore, a good visual inspection and interpretation are required on the reconstructed slices and the 3D volumes.

Fig. 6 shows 3 front views of the sample during the weathering process. After 10 days of exposure to the acid environment, a degradation of the external zone of the small cylindrical samples was noticeable on the reconstructed slices as it covered almost the entire sample. At the base of the sample which is attached to the carbon lead, almost no deterioration was present due to the impregnation and sheltering of the glue. The new gypsum layer was distinguishable from the carbonate-rich cement and quartz grains of the original stone material due to its lower X-ray attenuation, which depends on the atomic number and the density of the material, and thus slightly lower gray value.

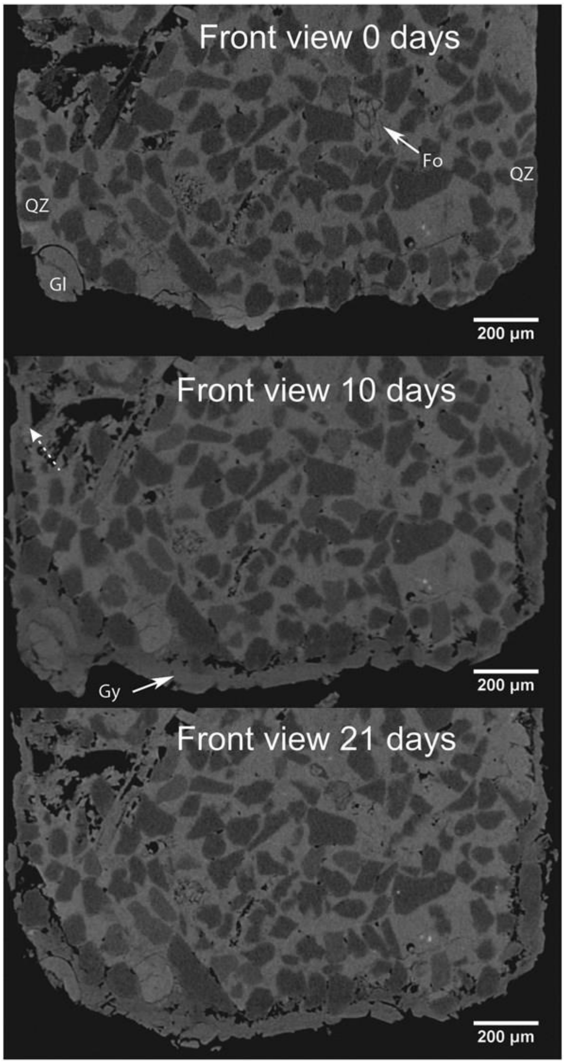

Fig. 6. Cross sections through Lede 1 sample (front view) before, after 10 and 21 days of weathering. The formation of gypsum crystals (Gy) is visible on the surface of the sample after 10 and 21 days. In addition, new pores are formed just below the crust and inside the sample. The latter is due to dissolution, covering and only partially infilling of notches with gypsum (dashed arrow). Other pores inside the sample like the elongated shell fragment (upper left) are closed. Also a foraminifer (white arrow) is filled with gypsum.

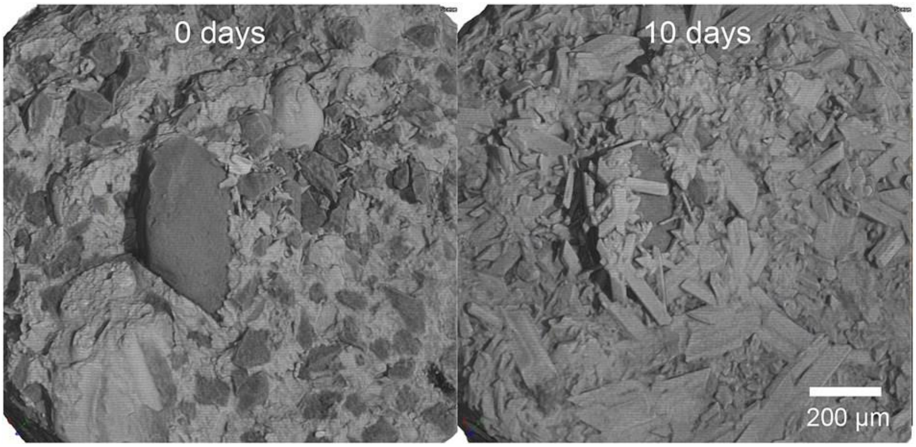

Fig. 7. 3D rendering of the surface of the Lede 1 sample. Left image before acid test; right image after 10 days in acid environment.

Just below the gypsum crust, a distinguishable coeval porous layer appears. Already after 10 days, several quartz (Qz) and glauconite (Gl) grains are incorporated into the crust. As can be seen on the front view in Fig. 6, a glauconite grain on the lower left corner is fully enclosed in the gypsum layer. Others are surrounded on their grain boundaries by micro-cracks and dissolution zones and are in this way becoming detached from the stone. Deeper inside the stone, two main features are noticeable on the cross sections. First, some of the initial notches present at the surface of the cylindrical core were, after 10 days, covered by gypsum crystals (upper left corner, dashed arrow), leaving an empty space in the center. The infilling of open pore structures and smaller dissolved fossil fragments, for example the elongated shell fragment, results in a reduction of the total porosity. Also, fossilized foraminifers (Fo) are partially to completely filled with secondary material, as indicated with an arrow on the figure.

After 21 days of exposure, the reconstructed 2D slices show that the gypsum layer has not grown much further with an almost similar thickness. However, it tends to flake off, leaving below a more cracked porous structure. In fact, the glauconite grain and part of the gypsum crust are almost fully removed from the stone surface. Fig. 6 also demonstrates that the infilling of already present pore structures stagnates; only a more cracked gypsum crust is shown.

By combining the different 2D slices, a 3D volume can be rendered. On those 3D rendered volumes, the euhedral gypsum crystals are visible (Fig. 7). Their tabular–prismatic habits are forming rosette-like structures on the surface of the sample. Some of the quartz grains are overgrown by gypsum crystals. Along a virtual cutting plane, pore structure evolution inside the sample can be observed (Fig. 8). In this way, a dissolution zone at the surface of the sample and around quartz grains is observable. By thresholding the pore structure in the samples, the internal network becomes visible as demonstrated in Fig. 9.

This figure represents the pore structure changes for the Lede 1 sample after10 days and 21 days of weathering. In the left column, the entire rendered volume is shown for the different steps, while in the furthest right column only the rendered pore structure is revealed. The red color represents the largest pores, the blue color the smallest ones. In the first row (initial situation) the red pore structure corresponds to an elongated, dissolved shell fragment. Around this big pore, some smaller pores are visible. In contrast, on the second row (weathered situation after 10 days) the red volume occupies less volume and new, relatively larger pores (in green) are formed on the edges of the sample. Finally, in the third row (weathered situation after 21 days) the large shell fragment becomes connected with the newly formed pore structure on the border, resulting in one large interconnected pore structure (red structure). Some newly formed smaller pores (blue) are visible on the border of the sample.

Generally, it should be noted that for the image analysis of the porosity changes, discussed in the next section, the formation of a porous layer below the crust, the formation of new pore structures and the infilling of already present pores are the main factors affecting the porosity. Those factors are crucial for the understanding and interpretation of the results.

3.2. Porosity measurements

3.2.1. Open, closed and total porosity measurements

Total, open and closed porosity were measured before weathering and after 10 and 21 days of weathering in the acid environment.

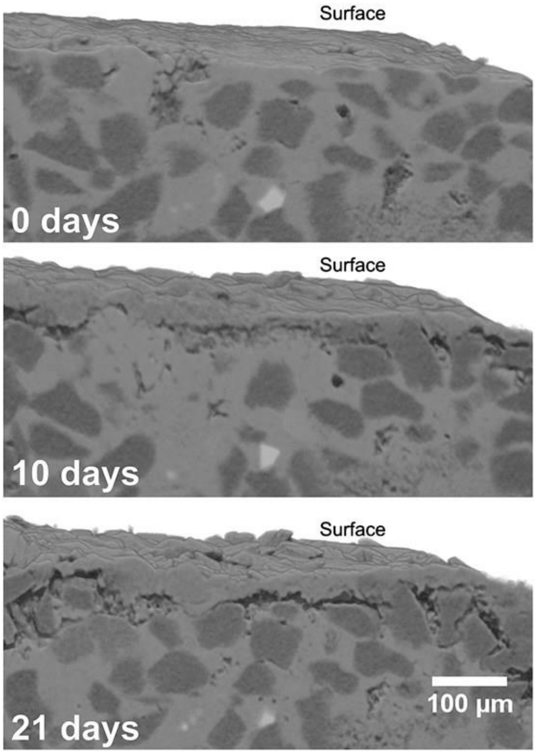

Fig. 8. 3D rendered volume along a cutting plane inside the weathered sample.

Fig. 10 demonstrates that the total porosity of the Lede 1 sample increased from 1.4% to 2.0% after 10 days and to 3.2% after 21 days. On the other hand, the total porosity of the Lede 2 sample increased from 0.4% to 1.8% and at the end of the test to 2.7% (Fig. 10). So for both samples, an increase in porosity is shown after 10 and 21 days. In addition, the ratio of open and closed porosity was calculated for both samples. That ratio is shown in dark gray for the open porosity and light gray for the closed porosity on the same graphs (Fig. 10). For both samples, the open porosity decreases after 10 days and increases again after 21 days. The open porosity for sample Lede 1 dramatically decreases from 60.4% to 10.0% after 10 days and increases to 74.0% after 21 days. A similar observation can be made from sample Lede 2. A significant decrease in open porosity is noticeable from 48.7% to 30.0% after 10 days and an increase to 45.2% after 21 days.

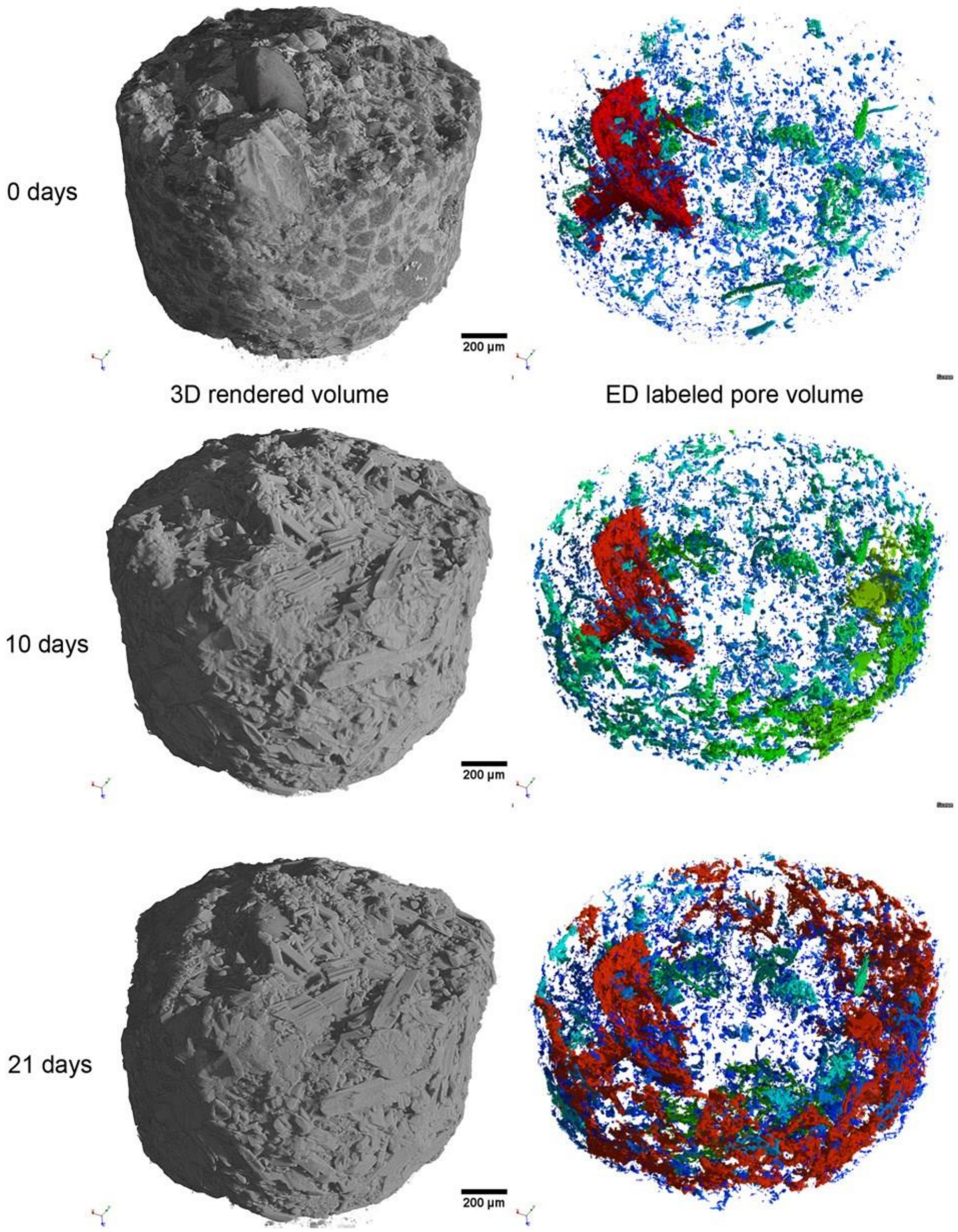

Fig. 9. 3D rendered volumes of the pore structure change of the Lede 1 sample. The first row represents the initial situation; the second row represents the weathered sample after 10 days and the last row shows the weathered sample after 21 days. In each row, the 3D rendered volume and the color-coded pore structure according to their equivalent diameter is shown. Red color-coded pores are the largest and blue are the smallest pores.

3.2.1. Partial and radial porosity measurements

The porosity calculated in a certain volume inside the sample, which can be as a function of the position or depth in the sample, is referring to the partial porosity. Fig. 11 shows the partial porosity as a function of the position in the x-direction, as described in Fig. 9. for the Lede 1 and Lede 2 samples. For both samples there is a great increase in porosity from the edges of the sample up to a depth of about 400 µm after 10 and 21 days. For the Lede 1 sample, the porosity on one edge changes from 0.5% to 4.2% after 10 days and 8.0% after 21 days. The Lede 2 sample shows the same trend, from almost no porosity to 4.2% after 10 days and 9.0% after 21 days. For the Lede 1 sample, the increase in porosity after 10 days is almost nil in the center of the sample, from 1.8% to 2.0% between 800 and 1600 µm. After 21 days, the figure shows an overall increase, from 2.0% to 3.0%. The graph for the Lede 2 sample demonstrates a strong overall increase of partial porosity after 10 days from 0.5% to 1.6% between 600 and 1400 µm and a slightly lower increase after 21 days (from 1.6% to 2.3%).

Similar to the Lede 1 sample, a large increase at the edges of the sample is visible. The partial porosity in the y-direction (Fig. 12) provides the same structural information as in the x-direction for both samples. The calculation of the partial porosity in the z-direction is presented in Fig. 13. Again, for both samples, the increase in porosity is the highest on the edge of the sample. For The Lede 1 sample, the average partial porosity between 0 and 600 µm increases from 1.0% to 2.2% after 10 days and 3.6% after 21 days. Between 0 and 400 µm, the average partial porosity of the Lede 2 sample increases from 0.3% to 2.6% after 10 days and 3.3% after 21 days. For Lede 1, after 10 days, there is a slight decrease in porosity inside the sample and after 21 days the porosity greatly increases

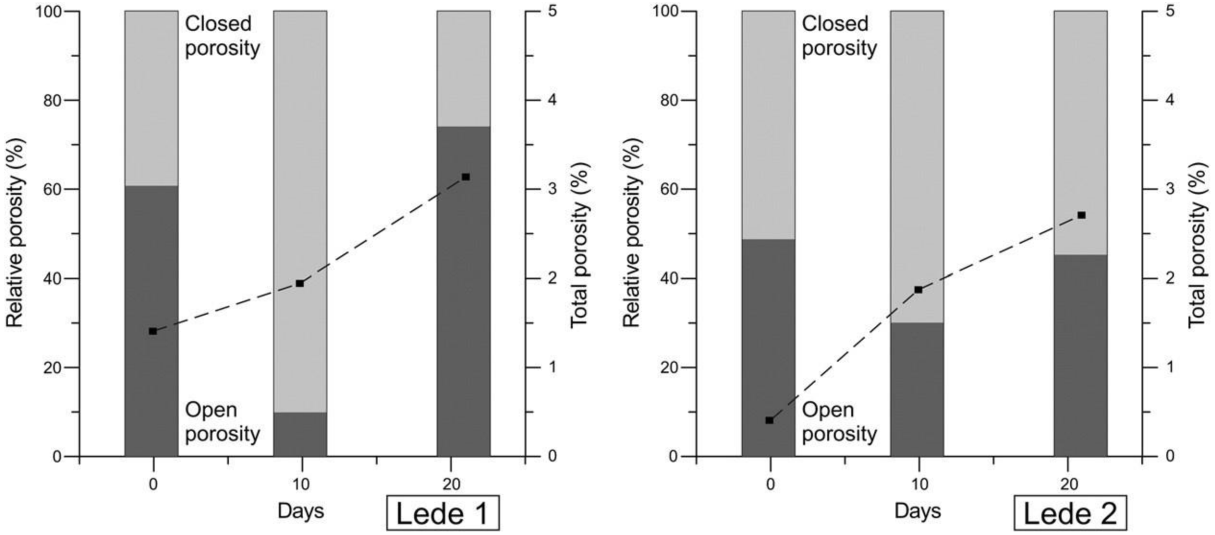

Fig. 10. Total porosity change and change of open and closed pore structures of the Lede 1 and Lede 2 samples at the beginning of the test, after 10 days and after 21 days. The total porosity is indicated by a dashed line. The relative open porosity is shown in dark gray and the relative closed porosity is shown in light gray

To avoid overestimated values due to geometrical factors on the edges of the samples, the radial porosity is also measured. Fig. 14 demonstrates that the affected zone for both samples is concentrated in the outer 200 µm of the sample and not in the 400 µm zone as registered with the partial volume measurements. Between 0 and 200 µm, the average radial porosity for the Lede 1 sample increases from 1.1% to 2.0% after 10 days and 3.2% after 21 days. In case of the Lede 2 sample, the average radial porosity increases from 0.3% to 2.1% after 10 days and 3.2% after 21 days.

3.2.3. Equivalent diameter measurements

It is interesting to compare the porosity results with the dimensional changes. Those changes can be obtained by measuring the equivalent diameter (ED) of each pore structure during the different steps of weathering. General trends observed are (1) an increase in ED after 21 days, (2) increase in amount of pores smaller than 100 µm after 21 days and (3) fragmentation of large pore structure after 10 days. Fig. 15 displays the measured ED in function of the volume percentage of the total pore volume. In addition, for each ED interval, the amounts of pores within that interval are given (number above the bar). Both volume percentage and amounts of pores are shown because they provide complementary information. A thousand small pores can occupy half of the total pore volume while, on the other hand, one large pore network can occupy the other half.

For example, for the Lede 1 sample, in the initial situation (black color on Fig. 15) there were 14,111 pores with an ED smaller than 100 µm, while one pore had an ED between 100 and 200 µm and another pore between 300 and 400 µm. Some 50% of the total porosity was attributed to the pores smaller than 100 µm, 48% to the pores between 300 and 400 µm and only 2% to the pore between 100 and 200 µm. As can be seen on the graph, after 10 days exposure, the pore structure significantly changed. The amount of pores with an ED smaller than 100 µm decreased to 12,421 but amounted to 54% of the total porosity. The two biggest pores had now an ED between 200 and 300 µm (31% of the total porosity). Pores with an ED between 100 and 200 µm increased to 8, contributing 15% of the total porosity.

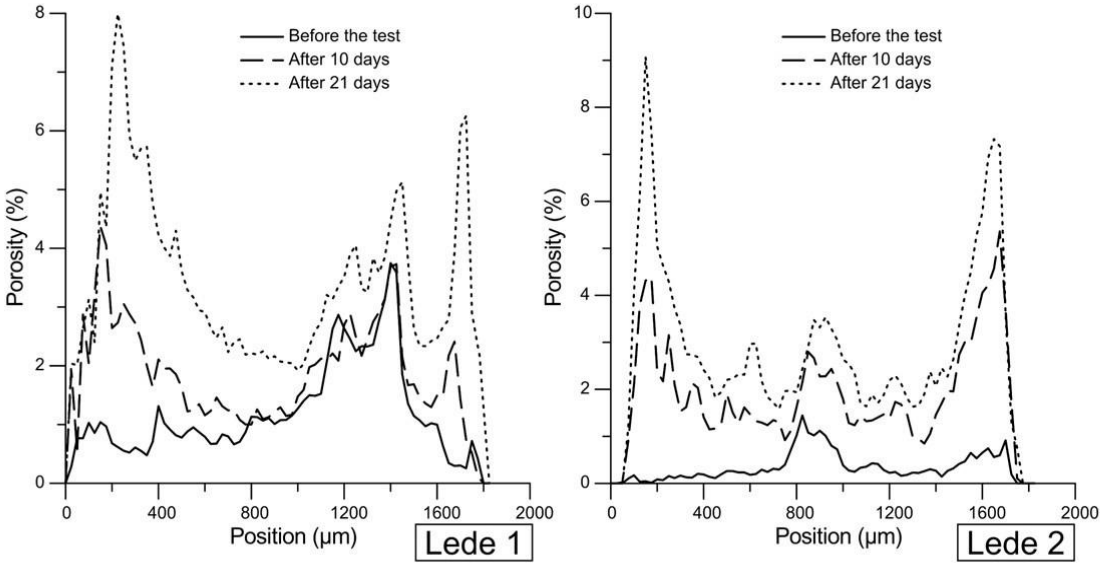

Fig. 11. Porosity in the x-direction for Lede 1 (left) and Lede 2 (right).

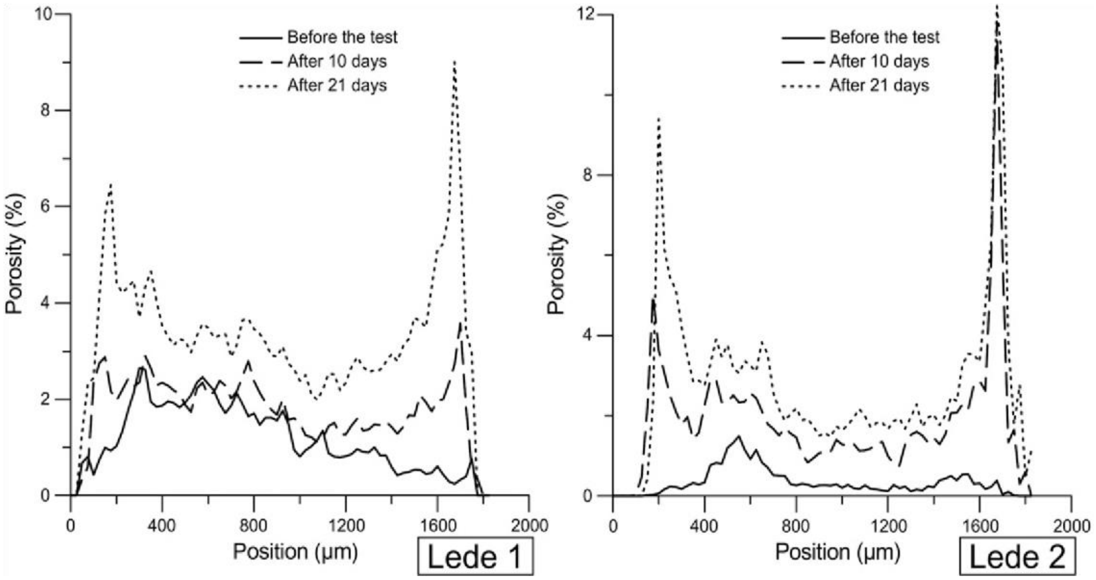

Fig. 12. Porosity in the y-direction for Lede 1 (left) and Lede 2 (right).

Finally, after 21 days, a drastic increase in ED is shown in the graph. One big pore was present with an ED between 400 and 500 µm and amounted to 60% of the total porosity. In the ED-interval of 100 to 200 µm, the number of pores decreased to two (only 5% of the total porosity). A significant increase in the amount of pores to 21,188 can be noted in the ED-interval smaller than 100 µm. The latter contributes 35% to the total porosity.

A similar trend is shown in the pore structure change of the Lede 2 sample. The only difference was the initial pore structure. This structure contained only pores (9937) smaller than 100 µm. After 10 days, six new pore structures are shown, amounting to 29% of its total porosity. After 21 days the frequency of the smallest pores significantly increases from 7245 to 13,873 and two bigger pore structures with ED ranging between 200 and 300 µm and 300–400 µm are visible. The overall trend seems similar as for sample Lede 1, but for the interpretation of those results a comparison with the visual interpretation is mandatory.

3.3. SEM and petrographic microscopy

SEM and thin section microscopy results were obtained on the final failed samples. 2D petrography of the samples revealed, as already observed with micro-CT, a gypsum layer (number 1 in Fig. 16), a porous layer below (number 2 in Fig. 16) and an unweathered, internal zone. As measured with a calibrated scale, the gypsum layer is between 0 and 100 µm thick and the porous zone is below 100 µm.

Several grains of the stones were detached from the cement whereas others showed a significant zone of dissolution on their boundaries. As well as in the gypsum crust as in the porous zone below, small parts of the original cement could be observed. Gypsum crystals were also revealed with SEM on the surface of the samples, covering some of the large quartz grains (Fig. 17) on the Lede 1 sample.

Smaller pore structures under 10 µm were visible between and inside larger gypsum crystals on the surface of the sample. On an internal surface of the Lede 1 sample, the same dissolved shell fragment as in Fig. 6, obtained with high resolution X-ray CT, could be observed (arrow on upper Fig. 18). As can be seen, the gypsum crystals were removed during the polishing process (arrow on the lower Fig. 18), but small parts of the gypsum were measured on the inner surface of the dissolute shell fragment (arrow upper figure).

4. Discussion

The aim of this study was to use X-ray CT to describe pore modifications during weathering processes as a function of time. The results described above provide a high-quality overview of structural pore rearrangements during crust formation obtained by high resolution X-ray CT and 3D image analysis. Variations in porosity, interconnectivity and dimensions were quantified as a function of time. It should be noted that visual qualitative observations on the 2D reconstructed slices and 3D rendered volumes already provided crucial structural information. Those observations are essential in the interpretation of the results obtained by image analysis. Visually, a coeval porous layer appears just below the crust, due to the dissolution of the cement and the covering of newly formed gypsum. This dissolution reaction with sulfur pollutants has been studied in detail in other studies (Cardell-Fernandez et al., 2002; Charola, 1987; Graedel, 2000). As well as dissolution of calcium carbonate also inducing micro-cracking inside glauconite grains, dissolution of cement around quartz grains and detachment of gypsum crystals are contributing to the origination of the porous layer. In Fig. 6, the slight detachment of the gypsum crust after 21 days is visible, especially in the zone around the glauconite (Gl).

Those structural changes are expected to be responsible for the increase in porosity due to weathering. In addition, the covering and partial infilling of notches at the surface of the sample can influence the total porosity after weathering. This is the case if the crust is an integral part of the original building stone. Bearing in mind that the notch was not a pore at the initial stage of the alteration this covering process will also be responsible for a general increase in porosity inside the sample. The dashed line in Fig. 6 indicates the covering of a notch and thus the formation of a new pore. In contrast, the infilling of larger pore structures such as the partially dissolved shell fragment and also smaller structures such as foraminifers will reduce the total porosity. Also the complete infilling of superficial notches will reduce the total porosity. The first gypsum layer formed after 10 days can prevent the $S0_2$ from attacking the calcareous cement again due to sheltering of the first formed gypsum crystals. The thickness of the gypsum layer does not increase by much after the second degradation step (Fig. 6).

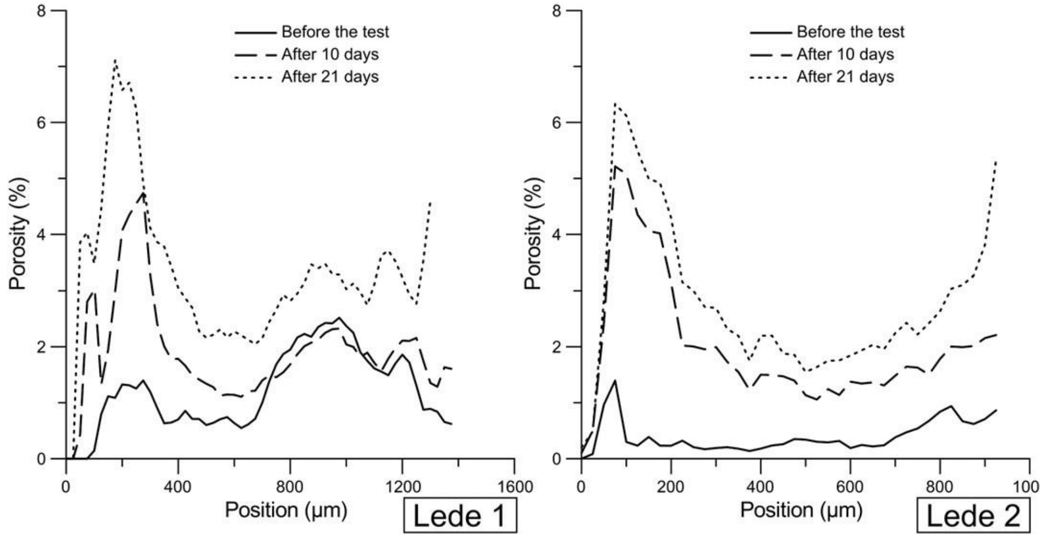

Fig. 13. Porosity in the z-direction for Lede 1 (left) and Lede 2 (right).

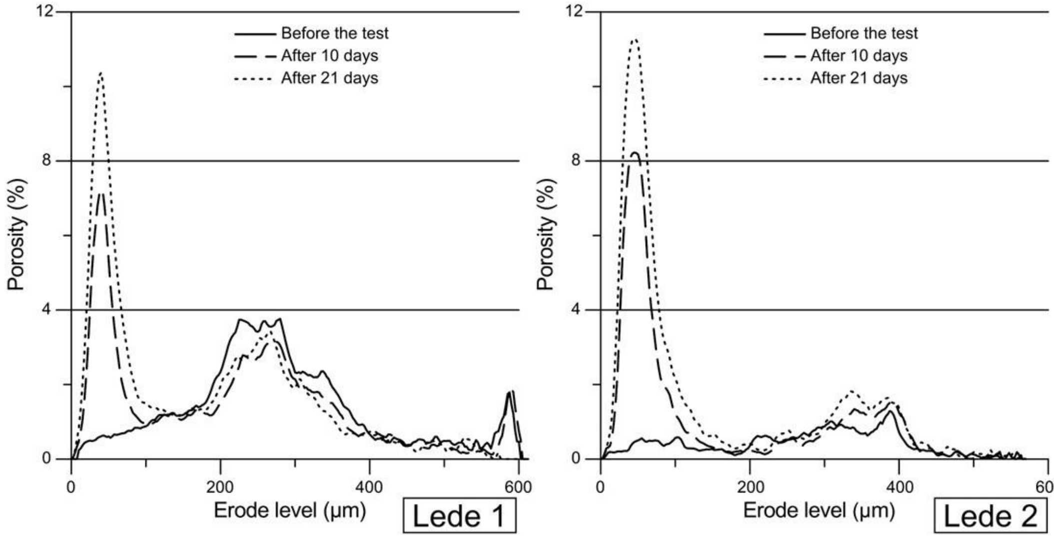

Fig. 14. Radial porosity for Lede 1 (left) and Lede 2 (right).

As can be seen from the Results, the overall total porosity of the samples will increase after 10 and 21 days although both reducing and increasing porosity processes are present and the gypsum crust was not growing much between 10 and 21 days. The change in pore structure after a second degradation step probably only depends on the cracking and slight removal of the first formed gypsum layer and formation of small pores on top of that crust, as have been observed with SEM. The difference between the rate of increasing porosity of the Lede 1 and Lede 2 sample lies in the amount of initial macro pores.

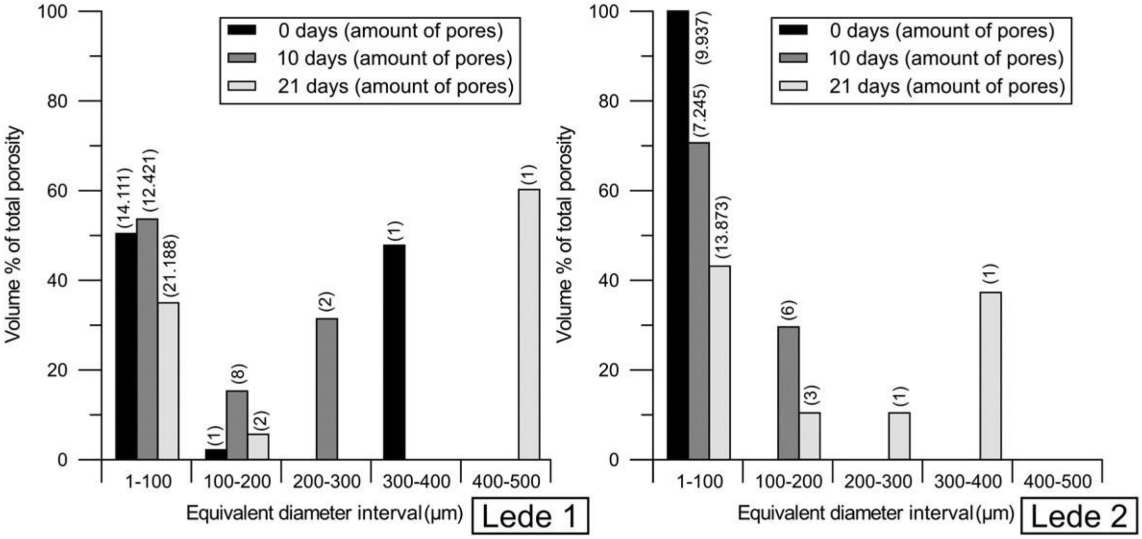

Fig. 15. Dimensional overview of the pore structure in the Lede 1 sample (left) and the Lede 2 sample (right). The volume percentage of the total porosity is given for each equivalent diameter interval after 0 days (black), 10 days (dark gray) and 21 days (light gray). On top of each bar, the total amount of pores is shown.

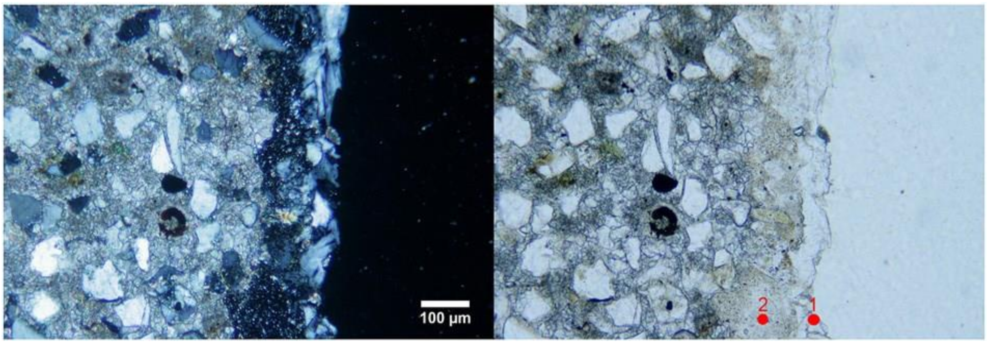

Fig. 16. Petrographic microscopy image of the final failed situation (on the left side crossed polarization and on the right side normal polarized transmitted light). The external gyp sum crust (1.) and porous zone below (2.) are detectible.

In Lede 1, one large open pore was present (a dissolved shell fragment). After 10 days, it was mostly filled with gypsum. This partial infilling process, combined with the newly formed porous layer below the crust, resulted in only a slight porosity increase in comparison with the Lede 2 sample. In the latter, only small pores were present and thus the infilling of the initial pore structure was limited. After 21 days, the infilling of the shell fragment in the Lede1 sample stagnated, probably due to the sheltering process of the first formed gypsum crystals and only the cracking and removal of the first formed gypsum crust played a significant role. This resulted in a higher porosity increase for the second degradation step, similar to the increase in the Lede 2 sample. The change in open and closed porosity during the experiments can be explained in combination with the visual interpretation. With regard to the Lede 1 sample, the big open pores (including the dissolved shell fragment) were fully covered with a gypsum layer, resulting in a high increase in closed porosity after 10 days. This can be seen in Fig. 6, indicated with a dashed arrow. By flaking off and cracking the previously formed gypsum layer after 21 days, the closed pores became connected again to the atmosphere. In addition, there is some evidence of pore coalescence and linking of micro cracks. As a consequence, the open porosity increased. Although the gypsum layer visually did not change much after 21 days in comparison with the situation after 10 days, the porosity change is significant. The same trend is visible in the Lede 2 sample, only the effect is less pronounced. This is attributed to the different, initial pore structure of both samples.

The partial porosity results obtained through image analysis indicate a porous zone up to a depth of about 400 µm after 10 and 21 days. This almost certainly corresponds to the newly formed porous layer below the gypsum crust and the pore structure in the gypsum crust itself. The slight increase in the center of the Lede 1 sample after 10 days indicates an equalization process between clogging and opening of new pore structures. The clogging process corresponds with the closure of the big shell fragment inside the sample. On the other hand, the dissolution process of the calcium carbonate cement contributes to the increase in porosity. After 21 days, the peel off of the gypsum layer increases again the porosity. According to the interpretation made in Fig. 5, the calculated value on the borders of the samples is overestimated, due to the geometrical factors. The calculated volumes change dramatically at the border of the sample. For that reason, radial porosity measurements were introduced and revealed a porous zone between 0 and 200 µm. Although radial porosity measurements are more reliable for measuring porosity changes on the edges of cylindrical structures, deeper inside the sample the regions of interest or shells become so small that the volume is not representative anymore. In addition, the shape of the regions of interest for the different volumes changes according to the external shape of the sample. If a volume of interest from a circle erodes several times, the new volume of interest will be different from a volume of interest derived from the eroding process of an irregular shape. This is the case if the surface of a smooth cylinder of stone is covered with random gypsum crystals.

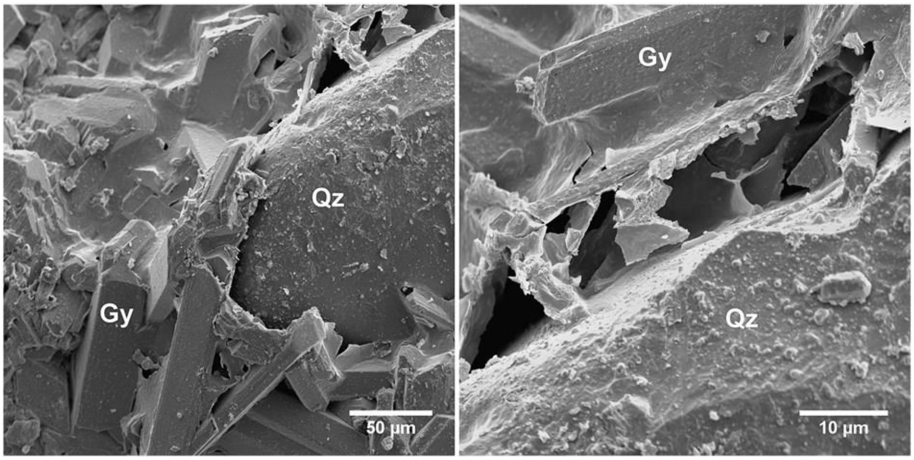

Fig. 17. SEM image of the surface of the Lede1 sample (Gy, gypsum crystals; Qz, quartz grains).

As a consequence, toward the center of the volume, the volume of interest of the sample after 10 days differs slightly from the volume of interest after 21 days. In the case of the Lede1 sample, one can assume that the decrease in porosity between 200 and 400 µm can be attributed to the infilling of the shell fragment, but in case of the Lede 2 sample there is no evidence for an increase in porosity between 300 and 400 µm. By plotting the volumes of interest on the original volumes it could be observed that, due to the gypsum crystals, the irregular volume of interest after 10 and 21 days occupied in the center more of the volume of the same large pore structure.

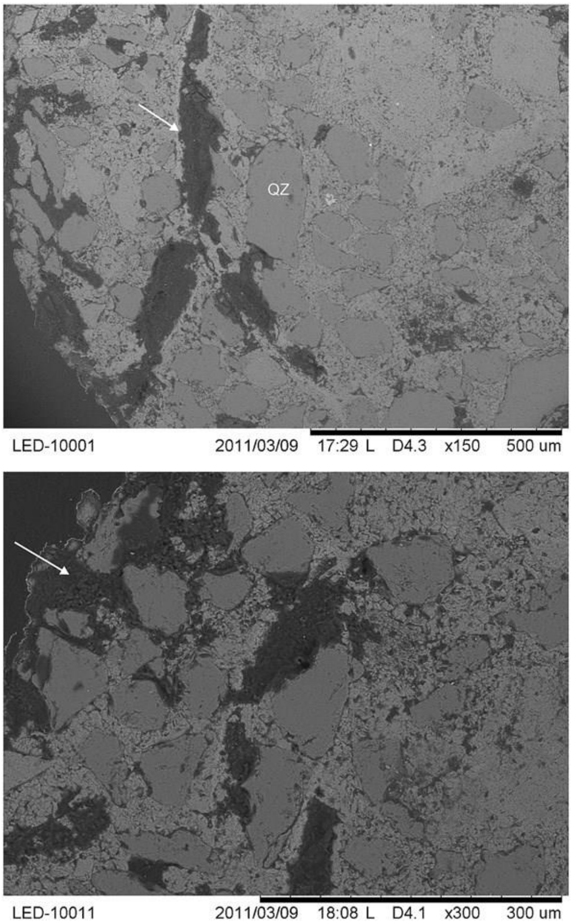

Fig. 18. SEM image of an internal surface of the Lede 1 sample after 21 days of weathering. Arrow on the upper figure indicates the gypsum layer inside the dissolved shell fragment. Arrow on the lower figure shows the removed gypsum layer due to polishing.

For the interpretation of the dimensional changes, a comparison with the visual interpretation is required (Fig. 9). It can be suggested that after 10 days of weathering, both big and small pore structures will become smaller due to gradual crystallization inside. For both samples, the amount of small pores (1–100 μm) decreases due to (1) complete infilling, (2) partial infilling so the pores become smaller than the resolution of the scan and (3) coalescence and thus resulting in larger (>100 μm) structures. With regard to the big pores, in the case of the Lede 1 sample, the equivalent diameter of the biggest pore (300–400 μm) also decreases due to partial infilling. Additionally, new relatively small pores (b300 μm) on the border of the sample will be formed. Those pores are located by radial porosity measurements between 0 and 200 μm deep from the border of the sample. Those pores are formed due to (1) coalescence of micro-pores, (2) partial infilling of larger pores, (3) micro-cracking around grains and (4) formation of new pores inside the zone of dissolution. After 21 days, the new pores formed after 10 days become connected to each other and create one big connected pore structure (>300 μm). In case of the Lede 1 sample, the dissolved shell fragment becomes connected with the porous layer below the crust and forms a pore structure with an ED between 400 and 500 μm. The striking increase of small pores (initial pores in the ED-interval lower than 100 μm are almost doubled) after 21 days can be attributed to the formation of new pores in the gypsum layer, as has been observed with SEM measurements. Remains of the original cement in the gypsum crust and just below were difficult to differentiate with X-ray CT because of similar X-ray attenuation coefficients with gypsum. However, with thin section microscopy those parts could be differentiated.

X-ray CT imaging turned out to be very valuable for both qualitative (visualization of dissolution processes, study of micro-crack initiation, pore infilling, etc.) and quantitative (calculation of partial porosity, estimation of dimensional changes, computation of interconnectivity, etc.) use during pore modification processes in a natural building stone in full 3D. Many previous studies have involved already real-time CT measurements of compression and unloading experiments (Geraud et al., 1998; Viggiani et al., 2004; Zhou et al., 2008), investigations of porosity changes before and after protective treatments (Bugani et al., 2008; Cnudde et al., 2004), bacterial weathering (De Graef et al., 2005) and time-lapsed micro structural imaging at synchrotron facilities in medical (Nazarian and Muller, 2004; Voide et al., 2009), as well as geomaterial applications. To the best of the author's knowledge, this study provides, for the first time, timelapse 3D quantification on micrometer resolution of specific weathering features. In addition, the approach outlined here relies on a combination of high resolution X-ray CT and image analysis that can be employed on a variety of rocks and weathering processes. Because water flow and thus also weathering depends very much on the pore structure inside materials, changing structures as described and quantified in this study are of the highest importance to better understand weathering processes which involve moisture or water. However, it should be noted that this study was primarily concerned with the time-lapsed quantification of changing pore structures in three dimensions. Although this quantification can improve the knowledge of weathering processes, some care must be taken when trying to make inferences from this study about realistic weathering processes. Pore modifications due to weathering are complex processes for which high resolution X-ray CT can provide a deeper insight but a variety of different processes are responsible for the alteration of the stone. In this study only SO_2 is taken into account while in realistic situations biological activity, temperature changes, rain, sheltering, airborne particles etc. can also play an important role (Ausset et al., 1999; Boke et al., 1999; RodriguezNavarro and Sebastian, 1996; Warscheid and Braams, 2000).

5. Conclusions

Weathering of natural building stones is a complex phenomenon. By introducing high resolution X-ray CT on artificial weathered samples, one can monitor structural 3D difference in function of time. In this way, every progression step can be evaluated using appropriate 3D image analysis software. The changing pore structure due to gypsum crust formation on the Lede stone, a calcareous sandstone, has been studied using X-ray CT. Fresh and weathered calcareous sandstones have been interpreted to obtain crucial quantitative, 4D micro-structural information on their pore structure modification. X-ray CT has been demonstrated to be a valuable technique to gain better insights into stone weathering characteristics. On both the 2D rendered slices and the 3D reconstructed volume, changes in pore structure due to gypsum crust formation were visible. Besides the visualization of the changing pore structure, the newly formed gypsum layer could also be visualized. Radial, partial, open and closed porosity were calculated in combination with their equivalent diameter. The results obtained from this induced weathering experiment on the Lede stone showed:

1. An increase in total porosity after 10 days of weathering in an acid(SO_2) environment and a decrease of open pore structures. After 21 days, the porosity still increases and the pore structure becomes open again.
2. Different partial porosity measurements were mandatory to locatethe changes in pore structure. In x-, y-, and z-directions there is an overestimation on the borders of a cylindrical sample, while radial porosity measurements provided specific information for changes on the surface of the sample. The structural changes were located on the edges of the over a thickness of 200 µm.
3. The interpretation of the structural changes was only possible incomparison with visual observations on the 3D rendered data and 2D reconstructed slices, linked with SEM and thin section microscopy. General trends observed

were an increase of ED and amount of pores smaller than 100 µm after 21 days and a fragmentation of large pore structure after 10 days.

Acknowledgments

The authors would like to thank the Agency for Promotion of Innovation by Science and Technology in Flanders, Belgium (IWT) for the PhD grant of J. Dewanckele.

References

Ausset P, Crovisier JL, DelMonte M, Furlan V, Girardet F, Hammecker C, et al. Experimental study of limestone and sandstone sulphation in polluted realistic conditions: the Lausanne Atmospheric Simulation Chamber (LASC) (vol 30, pg 3197, 1996). Atmos Environ 1996;30:R1-.

Ausset P, Del Monte M, Lefevre RA. Embryonic sulphated black crusts on carbonate rocks in atmospheric simulation chamber and in the field: role of carbonaceous fly-ash. Atmos Environ 1999;33:1525–34.

Boke H, Gokturk EH, Caner-Saltik EN, Demirci S. Effect of airborne particle on SO_2–calcite reaction. Appl Surf Sci 1999;140:70–82.

Brabant L, Vlassenbroeck J, De Witte Y, Cnudde V, Boone MN, Dewanckele J, et al. Three-dimensional analysis of high-resolution X-ray computed tomography data with Morpho. Microsc Microanal 2011;17:252–63.

Bugani S, Camaiti M, Morselli L, Van de Casteele E, Janssens K. Investigating morphological changes in treated vs. untreated stone building materials by X-ray microCT. Anal Bioanal Chem 2008;391:1343–50.

Camuffo D. Physical-weathering of stones. Sci Total Environ 1995;167:1-14.

Cardell-Fernandez C, Vleugels G, Torfs K, Van Grieken R. The processes dominating Ca dissolution of limestone when exposed to ambient atmospheric conditions as determined by comparing dissolution models. Environ Geol 2002;43:160–71. Charola AE. Acid-rain effects on stone monuments. J Chem Educ 1987;64:436–7.

Charola AE, Puhringer J, Steiger M. Gypsum: a review of its role in the deterioration of building materials. Environ Geol 2007;52:207–20.

Christe P, Turberg P, Labiouse V, Meuli R, Parriaux A. An X-ray computed tomographybased index to characterize the quality of cataclastic carbonate rock samples. Eng Geol 2011;117:180–8.

Cnudde V, Cnudde JP, Dupuis C, Jacobs PJS. X-ray micro-CT used for the localization of water repellents and consolidants inside natural building stones. Mater Charact 2004;53:259–71.

Cnudde V, Cwirzen A, Masschaele B, Jacobs PJS. Porosity and microstructure characterization of building stones and concretes. Eng Geol 2009a;103:76–83.

Cnudde V, Silversmit G, Boone M, Dewanckele J, De Samber B, Schoonjans T, et al. Multi-disciplinary characterisation of a sandstone surface crust. Sci Total Environ 2009b;407:5417–27.

Cnudde V, Boone M, Dewanckele J, Dierick M, Van Hoorebeke L, Jacobs P. 3D characterization of sandstone by means of X-ray computed tomography. Geosphere 2011;7: 54–61.

De Graef B, Cnudde V, Dick J, De Belie N, Jacobs P, Verstraete W. A sensitivity study for the visualisation of bacterial weathering of concrete and stone with computerised X-ray microtomography. Sci Total Environ 2005;341:173–83.

Dierick M, Masschaele B, Van Hoorebeke L. Octopus, a fast and user-friendly tomographic reconstruction package developed in LabView (R). Meas Sci Technol 2004;15:1366–70.

Dusar M, Dreesen R, De Naeyer A. Natuursteen in Vlaanderen, versteend verleden. 1st ed. Mechelen: Wolters Kluwer België NV; 2009.

Fobe B. Voorkomen, samenstelling en gebruik van de Balegemse steen. Bull Soc Belge Geol 1990;99–2:167–70.

Geraud Y, Mazerolle F, Raynaud S, Lebon P. Crack location in granitic samples submitted to heating, low confining pressure and axial loading. Geophys J Int 1998;133: 553–67.

Giavarini C, Santarelli ML, Natalini R, Freddi F. A non-linear model of sulphation of porous stones: numerical simulations and preliminary laboratory assessments. J Cult Herit 2008;9:14–22.

Graedel TE. Mechanisms for the atmospheric corrosion of carbonate stone. J Electrochem Soc 2000;147:1006–9.

Ketcham RA, Carlson WD. Acquisition, optimization and interpretation of X-ray computed tomographic imagery: applications to the geosciences. Comput Geosci 2001;27: 381–400.

Dewanckele J., De Kock T., Boone M.A., Cnudde V., Brabant L., Boone M.A, **FRONTEAU G.,** Van Hoorebeck L., Jacobs. P. 2012. 4D imaging and quantification of pore structure modifications inside natural building stones by means of high resolution X-ray CT. *Science of The Total Environment*. 416. p 436-448. https://doi.org/10.1016/j.scitotenv.2011.11.018

Maravelaki-Kalaitzaki P, Biscontin G. Origin, characteristics and morphology of weathering crusts on Istria stone in Venice. Atmos Environ 1999;33:1699–709.

Masschaele BC, Cnudde V, Dierick M, Jacobs P, Van Hoorebeke L, Vlassenbroeck J. UGCT: new X-ray radiography and tomography facility. Nucl Instrum Meth A 2007;580: 266–9.

Montana G, Randazzo L, Oddo IA, Valenza M. The growth of "black crusts" on calcareous building stones in Palermo (Sicily): a first appraisal of anthropogenic and natural sulphur sources. Environ Geol 2008;56:367–80.

Nazarian A, Muller R. Time-lapsed microstructural imaging of bone failure behavior. J Biomech 2004;37:55–65.

Nord AG, Holenyi K. Sulphur deposition and damage on limestone and sandstone in Stockholm city buildings. Water Air Soil Pollut 1999;109:147–62.

RodriguezNavarro C, Sebastian E. Role of particulate matter from vehicle exhaust on porous building stones (limestone) sulfation. Sci Total Environ 1996;187:79–91.

Rozenbaum O, Le Trong E, Rouet JL, Bruand A. 2-D image analysis: a complementary tool for characterizing quarry and weathered building limestone. J Cult Herit 2007;8:151–9.

Sabbioni C, Zappia G, Gobbi G. Carbonaceous particles and stone damage in a laboratory exposure system. J Geophys Res Atmos 1996;101:19621–7.

Siegesmund S, Torok A, Hupers A, Muller C, Klemm W. Mineralogical, geochemical and microfabric evidences of gypsum crusts: a case study from Budapest. Environ Geol 2007;52:369–81.

Smith BJ, Torok A, McAlister JJ, Megarry Y. Observations on the factors influencing stability of building stones following contour scaling: a case study of oolitic limestones from Budapest, Hungary. Build Environ 2003;38:1173–83.

Thomachot-Schneider C, Gommeaux M, Fronteau G. Modifications of the porous network of sandstone accompanying the formation of black varnish. Environ Geol 2008;56:571–82.

Torok A, Rozgonyi N. Morphology and mineralogy of weathering crusts on highly porous oolitic limestones, a case study from Budapest. Environ Geol 2004;46:333–49.

Viggiani G, Lenoir N, Besuelle P, Di Michiel M, Marello S, Desrues J, et al. X-ray microtomography for studying localized deformation in fine-grained geomaterials under triaxial compression. CR Mec 2004;332:819–26.

Vlassenbroeck J, Dierick M, Masschaele B, Cnudde V, Hoorebeke L, Jacobs P. Software tools for quantification of X-ray microtomography. Nucl Instrum Meth A 2007a;580: 442–5.

Vlassenbroeck J, Masschaele BC, Dierick M, Cnudde V, De Witte Y, Pieters K, et al. Recent developments in the field of X-ray nano- and micro-CT at the Centre for X-ray Tomography of the Ghent University. Microsc Microanal 2007b;13:184–5.

Voide R, Schneider P, Stauber M, Wyss R, Stampanoni M, Sennhauser U, et al. Timelapsed assessment of microcrack initiation and propagation in murine cortical bone at submicrometer resolution. Bone 2009;45:164–73.

Warke PA, Smith BJ. Complex weathering effects on durability characteristics of building stone. Geol Soc Spec Publ 2007;211–224:330.

Warscheid T, Braams J. Biodeterioration of stone: a review. Int Biodeter Biodegr 2000;46: 343–68.

Zhou XP, Zhang YX, Ha QL. Real-time computerized tomography (CT) experiments on limestone damage evolution during unloading. Theor Appl Fract Mech 2008;50:49–56.